
Influence of Carbon Microstructure on the Li-O₂ Battery First-Discharge Kinetics

Olivia Wijaya,^{a,b} Harry Hoster,^{a,c} Ali Rinaldi^{a,d,}*

^a TUM CREATE, 1 CREATE Way, Singapore

^b School of Material Science and Engineering, Nanyang Technological University, Singapore

^c Department of Chemistry, Lancaster University, Lancaster, LA1 4YB, United Kingdom

^d Department of Chemistry, King Fahd University of Petroleum & Minerals, Dhahran 31261, Saudi Arabia

* e-mail: rinaldi@kfupm.edu.sa

Abstract

Defects in the carbon microstructure have been reported to enhance the discharge performance of Li-O₂ battery. However, systematic studies correlating the presence of defects with the discharge kinetics have not addressed the variation of carbon electrode surface areas. In this work, carbon blacks and carbon nanofibers with different defect densities were investigated for their discharge properties. The electrolyte-accessible areas of the carbon electrodes were obtained from Cyclic voltammetry measurements. The microstructure and surface areas of the carbons were characterized by Raman spectroscopy, electron microscopy and N₂ isotherm. Linear sweep voltammetry and galvanostatic discharge experiments consistently demonstrated that graphitic carbons have more negative onset potentials and more negative discharge potentials at the same current density than defective carbons. The linear sweep voltammetry data were normalized to the carbon masses, BET surface areas and double layer capacitance-derived areas for comparison. Plot of inverse charge transfer resistance and double layer capacitance from electrochemical impedance spectroscopy measurements were used to extract current density values without knowledge of electrode areas. The current densities from impedance measurements exhibited good agreement with the data from linear sweep experiments. The electrochemical experiments conclusively showed that defects on the graphitic microstructure increase the discharge kinetics of the Li-O₂ battery.

Keywords: carbon defect, Li-O₂ battery discharge, electrochemical impedance spectroscopy, electrode area

1. Introduction

Aprotic Li-O₂ battery has attracted substantial research efforts in the recent years due its high theoretical specific energy. The theoretical specific energy of around 2000 Wh/kg could be achieved when discharged to Li₂O₂.^[1] However, numerous challenges have to be overcome to realize the Li-O₂ battery for the practical application. The paramount challenge for Li-O₂ is finding a stable electrolyte in the battery's highly oxidative environment. Stable air electrode that allows high specific capacity, power capability, and long cycle life is also a major challenge in Li-O₂ battery development. Thus far, the majority of research efforts employ porous carbons as the air electrodes due to their conductivity, low mass and high surface area to maximize the electrode-electrolyte interface for better kinetics and contain the discharge products. The capacity after the first discharge has been shown to correlate with the surface area of the carbon.^[2] The porosity of carbon electrodes also plays a role in determining the discharge capacity.^[3–5]

Defect sites including edges and functional groups on carbon surface have been reported to show catalytic effect toward O₂ reduction reaction (ORR) in various electrolytes.^[6–9] Yoo et al. reported that graphene nano sheet (GNS) demonstrated higher discharge voltage compared to the heat-treated GNS in Li-air battery using hybrid organic/aqueous electrolyte.^[8] Nakanishi et al. demonstrated that as-prepared cup stacked carbon nanotube (CSCNT) showed earlier ORR onset, superior discharge voltage, and capacity compared to heat-treated CSCNT in ionic liquid. ^[6,7] Our group also reported higher activity for oxidized carbon nanofibers compared to graphitized nanofibers in ether electrolyte.^[10] Nevertheless, the presence of defects on carbon has been reported to affect the cycle life and battery stability due to carbon oxidation and greater electrolyte decomposition.^[8,11–14] Although the role of defects have been demonstrated to increase the activity for ORR in metal-air battery, previous studies have not addressed the variation of carbon surface area when comparing carbons of different defect densities and morphologies.

In this study, we investigated carbon blacks and carbon nanofibers, representing two common carbon materials with different morphologies, as cathodes in the Li-O₂ battery discharge. First the carbons were characterized for their physical properties with electron microscopy, N₂ isotherm and Raman spectroscopy. Next, we compared carbon blacks and nanofibers with different graphitic degrees for their discharge kinetics in aprotic Li-O₂ battery cells. Linear sweep voltammetry (LSV), galvanostatic discharge and Electrochemical Impedance Spectroscopy (EIS) were used to investigate the discharge kinetics of the carbon materials. To compare the reactivity of carbons with different defect densities the data were normalized to the carbon surface area. We thus compared the surface area values obtained

from N_2 isotherm and double layer capacity (C_{DL}) measurements. Finally the plot of inverse charge transfer resistance (R_{CT}^{-1}) and C_{DL} extracted from Electrochemical Impedance Spectroscopy (EIS) measurements were employed to obtain the discharge kinetics trend of the various carbon electrodes. The method developed by Friedl et al. for porous carbon electrodes allows the determination of electrochemical kinetics without knowledge of the real electrode area.[15] The relation between defects on carbon materials and discharge properties was discussed.

2. Experimental

2.1. Chemicals and Experimental Setup

We employed two types of carbon materials in this work representing different morphologies and porosities. The first is commercial vapor grown carbon nanofibers from Pyrograf Products Inc., U.S.A. This group consists of PR24-HHT, subsequently referred as graphitized carbon nanofiber (G-CNF), PR24-LHT carbon nanofiber (CNF) and in-house chemically oxidized graphitized carbon nanofiber (Ox-G-CNF). G-CNF and CNF were annealed by the manufacturer at 3273 K and 1773 K respectively. The chemical oxidation was done by mixing G-CNF with concentrated HNO_3 for 12 hours at 383 K. The oxidized G-CNF was subsequently annealed at 1173 K for 3 hours in Argon environment using a tubular furnace to remove most of the functional groups. The second carbon type is commercial carbon black, which consists of graphitized acetylene black (G-AB) from Sigma-Aldrich and acetylene black (AB) from Alfa Aesar. The selection for the two carbon blacks were based on their similar surface areas and porosities to minimize variations in the cathode preparation. Similarly, the nanofiber samples were derived from the same parent material to achieve consistency in the fabricated cathodes.

Anhydrous 1,2-Dimethoxyethane (DME) and anhydrous lithium perchlorate ($LiClO_4$) (Sigma-Aldrich) were used as the electrolyte with the concentration of 0.1 M $LiClO_4$: DME. Anhydrous N-Methyl-2-pyrrolidone (Sigma-Aldrich) was used to dissolve the Polyvinylidene fluoride (PVDF) binder (HSV 900, Arkema) for cathode fabrication. The cell assembly and electrolyte preparation were performed in an Argon environment glovebox < 1 ppm of O_2 and < 1 ppm of H_2O . All the electrochemical experiments were conducted in ECC-Air cell fabricated by EL-Cell GmbH.[16] Prior to electrochemical testing the cells were allowed to rest for 12 hours in the Argon-filled glovebox. The O_2 flow was set to $0.015 \text{ ml min}^{-1}$. The electrochemical experiments were done in the laboratory room temperature at 295 K.

2.2. Electrode Preparation

The cathodes were prepared by coating mixture of the carbon powder with 20 wt% PVDF binder onto a Celgard 2320 separator. The coating was punched into 14 mm cathode disk. The cathode disk was then dried at 363 K for 12 hours inside a vacuum-sealed portable oven from Buchi, before being transferred to the glovebox. The typical carbon loadings were 0.4-0.5 mg cm⁻² for carbon black cathodes and 0.6-1.0 mg cm⁻² for carbon nanofiber cathodes. The typical electrode thickness was about 8 μm.

2.3. Physical Characterization

The carbon materials were characterized by using Witec Raman Spectrometer with the laser wavelength of 488 nm. Field Emission Scanning Electron Microscopes (FESEM) JEOL JSM-7600F and Transmission Electron Microscopes (TEM) JEOL 2100F were employed to observe the morphology of the carbon materials. Brunauer-Emmet-Teller (BET) surface areas were obtained from the analysis of N₂ isotherms performed at 77 K using Nova 3200e surface area and porosity analyzer from Quantachrome Instruments.

2.4. Electrochemical Characterization

Linear Sweep Voltammetry (LSV) and galvanostatic discharge experiments were performed using an Arbin Battery tester BT2000. LSV experiments were performed within the voltage range of 3.0 V to 2.5 V vs. Li/Li⁺ with 0.1 mV/s scan speed. The lower cut-off voltage for galvanostatic discharge is 2.0 V vs. Li/Li⁺. Cyclic Voltammetry (CV), and Electrochemical Impedance Spectroscopy (EIS) measurements were performed using a Biologic SP 200 potentiostat. CV measurements of fresh carbon cathodes were conducted in argon atmosphere within the voltage range of 3.1 V to 2.6 V vs. Li/Li⁺ at 20 mVs⁻¹ scan speed. EIS measurements were performed in a potentiostatic mode with a frequency range from 100 kHz to 10 mHz and AC amplitude of 10 mV. The charge transfer resistance (R_{CT}) and double layer capacity (C_{DL}) values were obtained by fitting with R + Q/R_{CT} equivalent circuit.[17] The fits were performed using EC-Lab software. The circuit elements are as follows: R is the sum of solution resistance and the charge transfer resistance of the Li anode, R_{CT} is the charge transfer resistance for the electrochemical reaction on the cathode and Q is the constant phase element representing C_{DL}.

3. Results and Discussion

3.1. Physical Characterization

Figure 1 shows the SEM images of the carbon materials used in this study. The carbon black sample shown in Figure 1a exhibits carbon spheres with diameter around 30 nm interconnected with a chain-like morphology. The G-CNF sample in Figure 1b shows the tubular morphology of the carbon filaments with an average diameter of about 85 nm. The hollow fibers are entangled forming agglomerates. More details on characterization of the fiber sample can be found elsewhere.[18,19]

Figure 2 shows the Raman spectra of the carbon powder samples used in this study. The G band at $\sim 1580\text{ cm}^{-1}$ corresponds to the in-plane Raman vibration mode of graphite. Meanwhile the D band at $\sim 1350\text{ cm}^{-1}$ corresponds to the lattice defects and edges of graphite. The intensity ratio of the D and G bands (I_D/I_G) indicates the degree of graphitic character in a carbon sample. The I_D/I_G values of the graphitized samples G-AB and G-CNF are lower than the AB and CNF samples, indicating more graphitic ordering of the carbon atoms and thus fewer defects in G-AB and G-CNF. The degree of graphitization of the carbon nanofiber samples are of the following order G-CNF (I_D/I_G 0.09) > Ox-G-CNF (I_D/I_G 0.18) > CNF (I_D/I_G 0.65). The Raman analysis also indicates that defects have been created on the graphitized sample after the chemical oxidative treatment (Ox-G-CNF). The bulk of the structure in the Ox-G-CNF is still graphitic as compared to the CNF sample. This is clearly observed in the moderate increase of I_D/I_G value after oxidation treatment.

Figure 3a and 3b show the high resolution TEM images of AB and G-AB carbon black respectively. The graphitized sample (G-AB) exhibits a more ordered concentric graphene layers as compared to the AB sample. The graphene layers in the AB sample have more bending and distortions indicating the presence of structural defects. The TEM observation is in qualitative agreement with the Raman spectroscopy measurement, revealing that the carbon microstructure in the graphitized sample has fewer imperfections or defects.

The N_2 adsorption-desorption isotherms and the calculated BET surface areas (A_{BET}) of the carbon powders are presented in Figure 4a and 4b. The isotherms in Figure 4a clearly show that G-AB and AB samples have very similar porosity and N_2 -accessible surface areas. The G-AB and AB carbon powders isotherms are almost an overlap especially in the $P/P_0 < 0.6$ region. The carbon black samples exhibit higher A_{BET} values than the nanofibers. The isotherms for G-AB, AB, and G-CNF powders show almost the absence of the hysteresis, which indicate the presence of mainly macropores. The oxidized sample

Ox-G-CNF has higher A_{BET} value and a clear hysteresis in the isotherm as compared to the G-CNF powder sample. This points out that the chemical oxidation treatment etched the G-CNF surface resulting in additional porosity and thus exposing more surfaces. The hysteresis at high P/P_0 tends to show that the Ox-G-CNF fibers are more entangled than G-CNF, very likely due to the presence of polar groups after the oxidative treatment.

The electrode form of the G-AB sample was also investigated with N_2 isotherms. The G-AB electrode containing PVDF binder was scratched out from the Celgard separator surface prior to the N_2 isotherm measurements. Figure 4a demonstrates the different isotherms of G-AB electrode and powder and the calculated A_{BET} values. The significant decrease in the A_{BET} value for the electrode form of G-AB can be attributed to surface or pore blockage by the PVDF binder. It is very likely that the N_2 isotherm; hence porosity and surface area values; depends on the electrode preparation method. Figure 4a clearly demonstrates that A_{BET} of the carbon powder is therefore not accurate to represent the electrolyte-accessible area of the electrode in the battery cell. Obtaining electrode surface area values from electrochemical method in the same electrolyte are therefore more relevant, and will be presented in the next section.

3.2. Electrochemical Measurements

Surface areas derived from C_{DL} measurements were calculated to obtain the electrochemistry-relevant values. The C_{DL} was obtained from the CV experiment of the carbon electrode in Ar-saturated 0.1M LiClO_4 in DME electrolyte. The details concerning the C_{DL} calculation from the CV data can be found in our previous work[17]. In brief, the C_{DL} value was calculated from the sum of cathodic and anodic currents at 2.8 V divided by twice the scan speed. The double layer-derived area (A_{CDL}) values were calculated according to equation 1:

$$C_{\text{DL}} = \varepsilon_0 \varepsilon_r A/t_{\text{DL}} \quad (1)$$

Where ε_0 the vacuum permittivity is $8.854\text{E-}6 \text{ Fm}^{-2}$, ε_r the relative permittivity for DME is 7.2 and t_{DL} the double layer thickness is 3.1 \AA . [20] The t_{DL} value was estimated from CV experiments of Glassy carbon disc-electrode (GC) with a diameter of 7 mm in Ar-saturated 0.1 M LiClO_4 DME electrolyte. The measured specific capacitance of the GC electrode is 0.203 F m^{-2} . The GC capacitance was then

used to calculate t_{DL} by using equation 1. The CV experiments and the C_{DL} , A_{CDL} values are presented in Figure 5 and Table 1 respectively. The overestimation of the A_{BET} areas is due to the better accessibility of N_2 molecules to carbon surfaces in comparison with the bigger size of solvated ions in the electrolyte. Furthermore in the electrode form some of the carbon surfaces maybe blocked by the binder.

It should be emphasized that the ratio of A_{BET} and A_{CDL} or rather the offset is not constant. Rather it varies with different type of samples. The origin of such differences may be due to the intrinsic surface properties and porosity of the carbons that affects e.g. electrolyte wetting and penetration to the pores. The electrode preparation method may also have an influence on the electrolyte wetted area due to the binder dispersion in the carbon matrix. Hence, extra care must be practiced in normalizing electrochemical kinetic parameters with BET surface areas especially when comparing various types of carbons.

Table 1 shows that the A_{CDL} values of the G-AB and AB are comparable. The similar electrode area values within the carbon blacks and nanofibers series of electrodes is beneficial when comparing the catalytic activity of these carbon electrodes. In particular our work focuses on the influence of defects in the carbon microstructure towards the discharge kinetics. It is thus crucial to keep the surface area and porosity constant when changing the amount of defects on the carbon electrode. The A_{CDL} values verify that the electrode areas in contact with the electrolyte for the same type of carbon material are indeed comparable.

We first examined the discharge behavior of the corresponding carbons in DME electrolyte by performing LSV and galvanostatic discharge experiments. DME was chosen as the solvent due to the high O_2 solubility.[21] Figure 6 presents the linear sweep voltammetry profiles of the carbon electrodes. The currents are normalized to the carbon mass in the electrode (Fig 6a), A_{CDL} from C_{DL} measurements (Fig 6b) and A_{BET} (Fig 6c). As shown in Figure 6 AB showed more positive reduction onset as compared to the graphitic sample G-AB. Correspondingly in Figure 6 CNF showed more positive onset potential as compared to the more graphitic G-CNF. Compared to G-CNF, the onset potential shifted to more positive value after the mild chemical oxidation in Ox-G-CNF. As depicted in Figure 6a, to reach a current of 50 mA g_c^{-1} AB electrode need to be polarized to about 2.74 V whereas G-AB need to be polarized to 2.6 V. From the linear sweep experiments the trend for the two types of carbons is consistent; graphitic carbons exhibit more negative onset potentials and lower current densities (at the

same polarization) compared with the more defective carbons. Furthermore, generating defects on carbon surface via chemical oxidation of the graphitic nanofiber enhances the discharge kinetics.

The A_{CDL} -normalized voltammograms in Figure 6b demonstrate that the graphitized carbons (G-CNF, G-AB) exhibit similar current densities and onset potentials despite the G-AB having 6-fold higher I_D/I_G value than G-CNF. This shows that the I_D/I_G value is merely indicative for the degree of graphitization in the carbon materials. In addition the Raman spectroscopy is not a surface-sensitive method to detect surface defects. Comparison of voltammetry profiles in Figure 6b and c highlighted the differences in presenting electrochemical data using electrode areas obtained from A_{CDL} and A_{BET} respectively. The current densities are one order of magnitude lower when normalized with A_{BET} . The differences in the LSV curves are obvious for CNF and AB. In A_{BET} -normalized curves, CNF is depicted to have slightly higher reactivity than AB at potentials lower than 2.65 V. Whereas in A_{CDL} -normalized curves, CNF showed slightly smaller current than AB. The A_{CDL} is more relevant parameter as it measures the carbon electrode area in the same electrolyte as the LSV, galvanostatic discharge and EIS experiments. The A_{BET} however is obtained from N_2 adsorption isotherm of the dry carbon powder.

The LSV curves can not be treated like a typical tafel plot. This is because in intermediate donor number solvent, such as DME, the Li_2O_2 discharge product grows on the carbon surface (surface mechanism) and away from the carbon surface (solution mechanism via the dissolved superoxide intermediate).[22] Both mechanisms will eventually block the carbon surface hindering the access of the electrolyte during the negative potential scan.

The effect of the carbon cathode microstructure to the discharge kinetics in aprotic solvent was further analyzed by performing galvanostatic discharge experiments. Figure 7 shows that the discharge potential at 50 mA g_c^{-1} for AB is higher than GAB electrode throughout the first discharge. The A_{CDL} -normalized discharge currents are 4.67 mA m^{-2} for GAB and 4.27 mA m^{-2} for AB. The A_{CDL} -normalized discharge currents were calculated by dividing 50 mA g_c^{-1} with the respective A_{CDL} values in Table 1. The slightly higher discharge current for G-AB does not account for the $\sim 120 \text{ mV}$ lower discharge potential as compared with AB at the beginning of discharge. The discharge profiles for the carbon nanofiber electrodes are shown in Figure 7b. The CNF and Ox-G-CNF electrodes clearly demonstrate higher discharge potential at 50 mA g_c^{-1} as compared to the G-CNF electrode. The galvanostatic discharge experiments are in good agreement with the LSV result indicating that graphitic

carbons exhibit poor discharge kinetics and that defects introduced to the graphitic carbon microstructure via chemical oxidation resulted in the enhancement of the discharge kinetics.

Of note, G-CNF electrode exhibited higher discharge capacity per A_{CDL} compared with more defective OX-G-CNF and CNF electrodes (Fig 7). The defect density on the carbon surface maybe partly responsible for the total discharge capacity of the cathode. Randomly distributed defect sites on carbon surface have been proposed to act as nucleation sites for Li_2O_2 . During discharge the lateral growth of Li_2O_2 will decrease the electrochemically active surface area which eventually lead to the passivation of the electrode. Increasing the amount of the defect sites will increase the Li_2O_2 nucleation rate leading to lower capacity.[23,24] It is thus not surprising that OX-G-CNF and CNF with higher I_D/I_G values demonstrated lower discharge capacities per A_{CDL} than the more graphitic G-CNF. The same argument may apply when comparing the discharge capacity per A_{CDL} of G-AB and G-CNF. G-AB exhibited lower capacity per A_{CDL} than the more graphitic G-CNF. This is despite the latter having higher A_{BET} and A_{CDL} values. Further studies are required to validate the argument proposed herein.

EIS experiments were also performed to study the influence of carbon microstructure to the discharge kinetics. Figure 8a and b are the impedance spectra presented in Nyquist and Bode plot for AB and G-AB electrodes under applied DC bias of 2.6 V. The first semicircle at high frequency (~1000 Hz) is attributed to the Lithium anode/electrolyte interface. The second semicircle at about 0.4 Hz is attributed to the O_2 reduction on the carbon cathode.[17] From the impedance spectra the charge transfer resistance (R_{CT}) and C_{DL} values were extracted from fitting the impedance spectra with the equivalent circuit (Figure 8a). Due to the non-ideal nature of the porous carbon electrode, constant phase element (Q) was used instead a simple capacitor to represent C_{DL} in the equivalent circuit to fit the impedance spectra.

The EIS method has its merits for being a transient method to analyze O_2 reduction discharge kinetics on various carbon electrodes. The transient method resulted in only a minimum amount of discharge product deposited on the carbon surface. Hence on the cathode side, the interface is still predominantly carbon surface-electrolyte interface.

The impedance parameters obtained from the fit with the equivalent circuit were used to establish a linear plot of inverse charge transfer resistance (R_{CT}^{-1}) versus C_{DL} for each type of carbon. From the slope of the linear curve, the current densities (j) in Am^{-2} for the carbon electrodes can be extracted without knowledge of the electrode areas accessible to the electrolyte (equation 2). The detail of the method can be found in the work by Friedl et al. [25]

$$R_{CT}^{-1} = \frac{n \cdot F \cdot t_{DL}}{R \cdot T \cdot \epsilon_r \cdot \epsilon_0} j \cdot C_{DL} \quad (2)$$

The formula is obtained from simplification of cylindrical capacitor equation to that of a plate capacitor, assuming t_{DL} is much smaller than the radius of one carbon particle. Since all of the electrodes were tested on the same electrolyte (same $\epsilon_r \cdot \epsilon_0$) and undergo the same O_2 reduction reaction, we can safely assume that apart from j the other values in the equation are constant.

In Figure 8c and d the values for R_{CT}^{-1} versus C_{DL} obtained from the EIS spectra for each type of carbon electrode is linearly fitted. The slopes of linear fit for the carbon electrodes are shown in Table 1. The slope for G-AB, the graphitic carbon black sample, is $0.59 (\text{F}\Omega)^{-1}$ which convert to current density of 0.0031 Am^{-2} . Whereas the more defective AB electrode has about 6-fold higher slope than G-AB at $3.48 (\text{F}\Omega)^{-1}$ and current density of 0.018 Am^{-2} . The trend is similar for the nanofiber samples; CNF electrode exhibits about 6-fold higher current density than G-CNF. After the chemical oxidation treatment the graphitic nanofiber demonstrates an increase of 6.8-fold in current density from 0.0019 Am^{-2} for G-CNF to 0.013 Am^{-2} for Ox-G-CNF. To note, Ox-G-CNF has similar current density value with CNF albeit 3.6-fold lower I_D/I_G value. The lower I_D/I_G value for Ox-G-CNF suggests that the bulk microstructure is still very graphitic after the oxidation treatment compared to the CNF bulk microstructure. It is plausible that the defects in Ox-G-CNF are located preferentially on the outer layers of the nanofibers. Whereas in CNF the defects are present throughout the bulk.

The current densities extracted from the transient EIS method were compared with the current densities values from A_{CDL} -normalized voltammetry curves (Table 1). The values are in the same order of magnitude, with marginally higher values for current densities from the LSV experiments. The discrepancies between EIS and LSV can be due to error in area estimation from A_{CDL} and/or different discharge kinetics between fresh carbon surface (EIS) and on the carbon surfaces with some Li_2O_2 coating (linear sweep). In general the positive effect of defects to the discharge kinetics observed from

the R_{CT}^{-1} versus C_{DL} plots is in good agreement with the LSV and galvanostatic experiments. The obvious advantage of the method developed by Friedl et al. is that the electrolyte-accessible and electronically-connected carbon area is inherently included in the R_{CT}^{-1} versus C_{DL} plot. Especially for porous electrodes the actual electrode area is often an unknown variable.

The electrochemical methods performed herein strongly point to the role of defects on graphitic carbon surface to increase the discharge kinetics in aprotic Li-O₂ battery. This is in agreement with previous works suggesting that edge structures, including defects improve the O₂ reduction reaction in non-aqueous Li-O₂ battery and acid media.[6,7,26] It has been discussed in literature that the electrocatalytic activity of carbon electrodes can be caused by the availability of specific adsorption sites or the density of electronic states (charge carriers). Defects on the basal plane have been shown to increase the kinetics of various redox systems.[27,28] Under constant current polarization, carbon surface with high defect density per area will result in low current per active sites, thus decreasing the reaction overpotential.

It must be stressed here that defects in this paper refers to disorder in the basal plane of graphite, which includes holes, steps, and edges. This work however does not try to cover the role of specific surface functional groups to the discharge kinetics and nor does answer whether the defects enhances the kinetics via specific surface interaction with the O₂, O₂⁻ or LiO₂. However, it is important to note that the Ox-G-CNF sample was annealed in an inert atmosphere at 1173 K to remove most of the functional groups prior to electrode fabrication. Further in-depth study is needed to better quantify the surface defects e.g. by temperature programmed desorption (TPD).[29,30] This work also does not cover the interface between carbon surface and discharge product. Whether the defects act as nucleation sites for Li₂O₂ or continue to be accessible to the electrolytes throughout discharge still require further investigation. Thorough electron microscopy studies of the discharge product on graphitic and defective carbons in the beginning of the first discharge step should be explored for future work investigations.

4. Conclusion

We presented a systematic investigation of carbon materials representing different defect densities as cathodes in aprotic Li-O₂ battery cells. Carbon black and carbon nanofiber cathodes were analyzed for their discharge kinetics by linear sweep voltammetry (LSV), galvanostatic discharge and EIS measurements. Presenting the data by normalizing with the carbon mass is inadequate, this is because

thermal annealing and chemical oxidation can result in the change of carbon surface area. We demonstrate that the electrolyte-accessible area values (A_{CDL}), obtained from C_{DL} measurements, show significantly different values from their respective BET area values (A_{BET}). Consequently the data presented by either the carbon mass, A_{CDL} or A_{BET} normalization show different values. The A_{CDL} values however are more relevant parameters to present the electrochemical results as they are measured in the same electrolyte. The LSV and galvanostatic discharge experiments from carbon blacks and carbon nanofiber electrodes consistently demonstrate that graphitic carbons show more negative onset potentials and more negative discharge potentials at the same current density than defective carbons. EIS measurements were performed to construct the plot of R_{CT}^{-1} versus C_{DL} for each carbon samples. This method allows the determination of the current density from the slope of the linear fit without knowledge of the electrode area. Defective carbons have steeper slopes and thus higher current densities than graphitic carbons. Although our conclusion is similar to previous authors, it differs substantially in three aspects: first is the role of electrode area in presenting the reactivity of carbon samples. Second, this study used carbon materials after thermal and chemical treatments from the same parent material to minimize morphological and surface area variations. And finally, this study used transient (EIS) and continuous (LSV and galvanostatic discharge) electrochemical methods to analyze the role of carbon defects on the Li-O₂ battery discharge kinetics.

5. Acknowledgements

This research programme is funded by the National Research Foundation Singapore under its Campus for Research Excellence and Technological Enterprise (CREATE) programme. The authors thank Dr. Jochen Friedl for insightful discussions.

References

1. Lu, Y.-C., Gallant, B. M., Kwabi, D. G., Harding, J. R., Mitchell, R. R., Whittingham, M. S. & Shao-Horn, Y. 2013 Lithium-Oxygen Batteries: Bridging Mechanistic Understanding and Battery Performance. *Energy Environ. Sci.* **6**, 750. (doi:10.1039/c3ee23966g)
2. Meini, S., Piana, M., Beyer, H., Schwammlein, J. & Gasteiger, H. A. 2012 Effect of Carbon Surface Area on First Discharge Capacity of Li-O₂ Cathodes and Cycle-Life Behavior in Ether-Based Electrolytes. *J. Electrochem. Soc.* **159**, A2135–A2142. (doi:10.1149/2.011301jes)
3. Yang, X., He, P. & Xia, Y. 2009 Preparation of mesocellular carbon foam and its application for lithium/oxygen battery. *Electrochem. commun.* **11**, 1127–1130. (doi:10.1016/j.elecom.2009.03.029)
4. Kuboki, T., Okuyama, T., Ohsaki, T. & Takami, N. 2005 Lithium-air batteries using hydrophobic

-
- room temperature ionic liquid electrolyte. *J. Power Sources* **146**, 766–769. (doi:10.1016/j.jpowsour.2005.03.082)
5. Cheng, H. & Scott, K. 2010 Carbon-supported manganese oxide nanocatalysts for rechargeable lithium–air batteries. *J. Power Sources* **195**, 1370–1374. (doi:10.1016/j.jpowsour.2009.09.030)
 6. Nakanishi, S., Mizuno, F., Nobuhara, K., Abe, T. & Iba, H. 2012 Influence of the carbon surface on cathode deposits in non-aqueous Li–O₂ batteries. *Carbon N. Y.* **50**, 4794–4803. (doi:10.1016/j.carbon.2012.06.003)
 7. Nakanishi, S., Mizuno, F., Abe, T. & Iba, H. 2012 Enhancing Effect of Carbon Surface in the Non-Aqueous Li-O₂ Battery Cathode. *Electrochemistry* **10**, 783–786. (doi:dx.doi.org/10.5796)
 8. Yoo, E. & Zhou, H. 2011 Li-air rechargeable battery based on metal-free graphene nanosheet catalysts. *ACS Nano* **5**, 3020–3026. (doi:10.1021/nn200084u)
 9. Black, R., Adams, B. & Nazar, L. F. 2012 Non-Aqueous and Hybrid Li-O₂ Batteries. *Adv. Energy Mater.* **2**, 801–815. (doi:10.1002/aenm.201200001)
 10. Rinaldi, A., Wang, Y., Tan, K. S., Wijaya, O. & Yazami, R. 2014 Lithium-air batteries for medium and large-scale energy storage. In *Advances in Batteries for Medium and Large-Scale Energy Storage* (eds C. Menictas M. Skyllas-Kazacos & T. M. Lim), pp. 419–430. Cambridge: Woodhead Publishing.
 11. Ottakam Thotiyl, M. M., Freunberger, S. a., Peng, Z. & Bruce, P. G. 2013 The carbon electrode in nonaqueous Li-O₂ cells. *J. Am. Chem. Soc.* **135**, 494–500. (doi:10.1021/ja310258x)
 12. Lu, J. et al. 2013 A nanostructured cathode architecture for low charge overpotential in lithium-oxygen batteries. *Nat. Commun.* **4**, 2383. (doi:10.1038/ncomms3383)
 13. Kang, S. J., Mori, T., Narizuka, S., Wilcke, W. & Kim, H.-C. 2014 Deactivation of carbon electrode for elimination of carbon dioxide evolution from rechargeable lithium-oxygen cells. *Nat. Commun.* **5**, 3937. (doi:10.1038/ncomms4937)
 14. Itkis, D. M. et al. 2013 Reactivity of carbon in lithium-oxygen battery positive electrodes. *Nano Lett.* **13**, 4697–701. (doi:10.1021/nl4021649)
 15. Friedl, J., Bauer, C. M., Rinaldi, A. & Stimming, U. 2013 Electron transfer kinetics of the – Reaction on multi-walled carbon nanotubes. *Carbon N. Y.* **63**, 228–239. (doi:10.1016/j.carbon.2013.06.076)
 16. http://el-cell.com/wp-content/uploads/manuals/ECC_AIR_manual.pdf In press. Electrochemical Test Cell ECC-AIR.
 17. Rinaldi, A., Wijaya, O., Hoster, H. E. & Yu, D. Y. W. 2014 History Effects in Lithium-Oxygen Batteries: How Initial Seeding Influences the Discharge Capacity. *ChemSusChem* **7**, 1283–1288. (doi:10.1002/cssc.201300986)
 18. Tessonier, J.-P. et al. 2009 Analysis of the structure and chemical properties of some commercial carbon nanostructures. *Carbon N. Y.* **47**, 1779–1798. (doi:10.1016/j.carbon.2009.02.032)
 19. Rinaldi, A. 2010 Synthesis of Carbon Nanotubes on Carbon Supports and the Purification of Carbon Nanotubes.
 20. Laoire, C. O., Mukerjee, S., Abraham, K. M., Plichta, E. J. & Hendrickson, M. A. 2010 Influence of Nonaqueous Solvents on the Electrochemistry of Oxygen in the Rechargeable Lithium–Air Battery. *J. Phys. Chem. C* **114**, 9178–9186. (doi:10.1021/jp102019y)
 21. Cormac O. Laoire and K. M. Abraham*, S. M. 2010 Influence of Nonaqueous Solvents on the

-
- Electrochemistry of Oxygen in the Rechargeable Lithium-Air Battery. *J. Phys. Chem.* **114**, 9178–9186.
22. Johnson, L. et al. 2014 SI The role of LiO₂ solubility in O₂ reduction in aprotic solvents and its consequences for Li–O₂ batteries SI. *Nat. Chem.* **6**, 1091–1099. (doi:10.1038/nchem.2101)
 23. Lau, S. & Archer, L. A. 2015 Nucleation and Growth of Lithium Peroxide in the Li–O₂ Battery. *Nano Lett.* **15**, 5995–6002. (doi:10.1021/acs.nanolett.5b02149)
 24. Rinaldi, A., Wijaya, O. & Hoster, H. E. 2016 Lithium-Oxygen Cells : An Analytical Model to Explain the Key Features in the Discharge Voltage Profiles. *ChemElectroChem* (doi:10.1002/celec.201600184)
 25. Friedl, J., Bauer, C., Rinaldi, A. & Stimming, U. 2013 Electron transfer kinetics of the VO₂⁺/VO₂²⁺ - reaction on multi-walled carbon nanotubes. *Carbon N. Y.* **63**, 228–239. (doi:10.1016/j.carbon.2013.06.076)
 26. Zheng, J.-S., Zhang, X.-S., Li, P., Zhou, X.-G. & Yuan, W.-K. 2008 Microstructure effect of carbon nanofiber on electrocatalytic oxygen reduction reaction. *Catal. Today* **131**, 270–277. (doi:10.1016/j.cattod.2007.10.104)
 27. Cline, K. K., McDermott, M. T. & McCreery, R. L. 1994 Anomalously Slow Electron Transfer at Ordered Graphite Electrodes: Influence of Electronic Factors and Reactive Sites. *J. Phys. Chem.* **98**, 5314–5319. (doi:10.1021/j100071a023)
 28. McCreery, R. L. & McDermott, M. T. 2012 Comment on electrochemical kinetics at ordered graphite electrodes. *Anal. Chem.* **84**, 2602–5. (doi:10.1021/ac2031578)
 29. Rinaldi, A., Zhang, J., Frank, B., Su, D. S., Abd Hamid, S. B. & Schlögl, R. 2010 Oxidative Purification of Carbon Nanotubes and Its Impact on Catalytic Performance in Oxidative Dehydrogenation Reactions. *ChemSusChem* **3**, 254–260. (doi:10.1002/cssc.200900179)
 30. Rinaldi, A., Frank, B., Su, D. S., Hamid, S. B. A. & Schlögl, R. 2011 Facile Removal of Amorphous Carbon from Carbon Nanotubes by Sonication. *Chem. Mater.* **23**, 926–928. (doi:10.1021/cm103069z)

Table 1. Summary of the physical and electrochemical properties of the carbon samples.

Sample	I_D/I_G <i>Raman</i>	$A_{BET}^{\#}$ ($m^2 g_c^{-1}$)	A_{CDL}^{**} ($m^2 g_c^{-1}$)	C_{DL} (CV) ($F g_c^{-1}$)	Slope* ($F\Omega$) ⁻¹	j^* (Am^{-2})	$j^{\#}$ (Am^{-2})
G-AB	0.57	75.4	10.7	2.17	0.59	0.0031	0.0046
AB	1.02	75.6	11.7	2.37	3.48	0.018	0.038
G-CNF	0.09	37.5	7.4	1.5	0.37	0.0019	0.0027
Ox-G-CNF	0.18	52	8.56	1.74	2.47	0.013	0.017
CNF	0.65	36.7	8.2	1.7	2.06	0.011	0.027

[#]Carbon

Powder measurements ** from equation 1 *from equation 2 #from Figure 6b at 2.6 V

Errors are not shown, but they are less than 10% for A_{BET} and 5% for C_{DL} measurements.

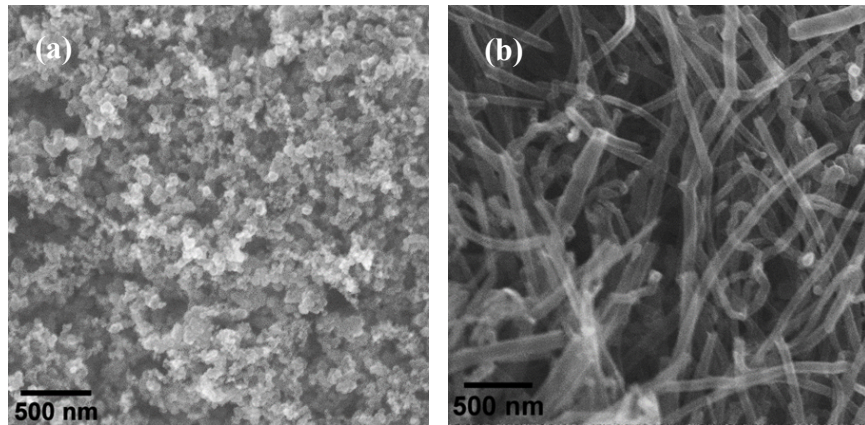


Fig. 1. SEM images of carbon black and carbon nanofiber powder samples: (a) G-AB and (b) G-CNF.

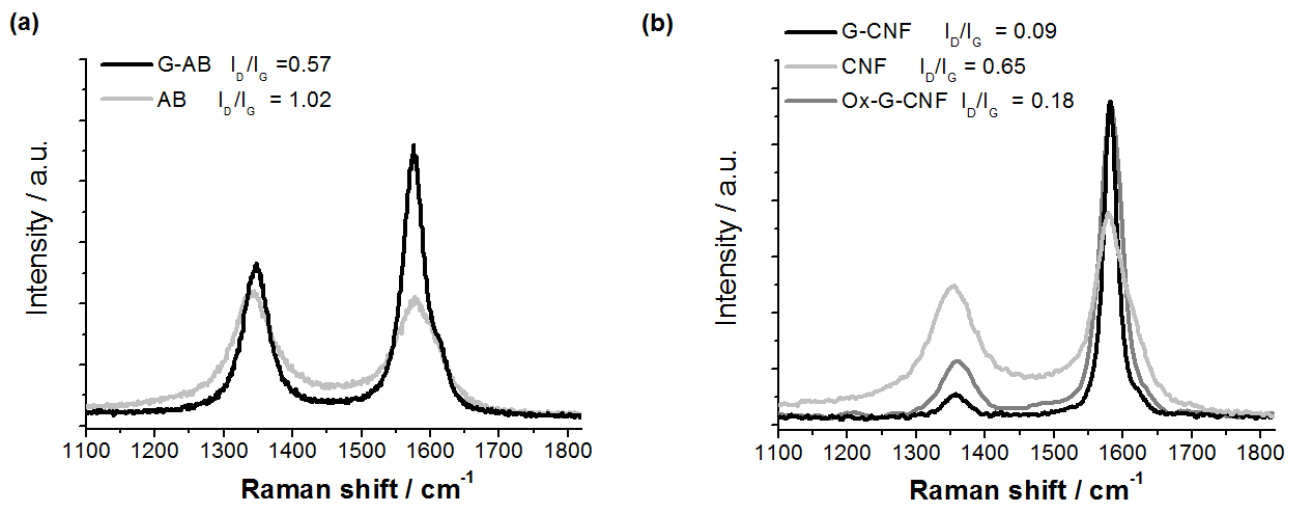


Fig. 2. Raman spectra of (a) carbon black and (b) carbon nanofiber powder samples. The graphitized samples exhibit higher intensity of the G-band at 1580 cm^{-1} compared to the more defective carbon samples.

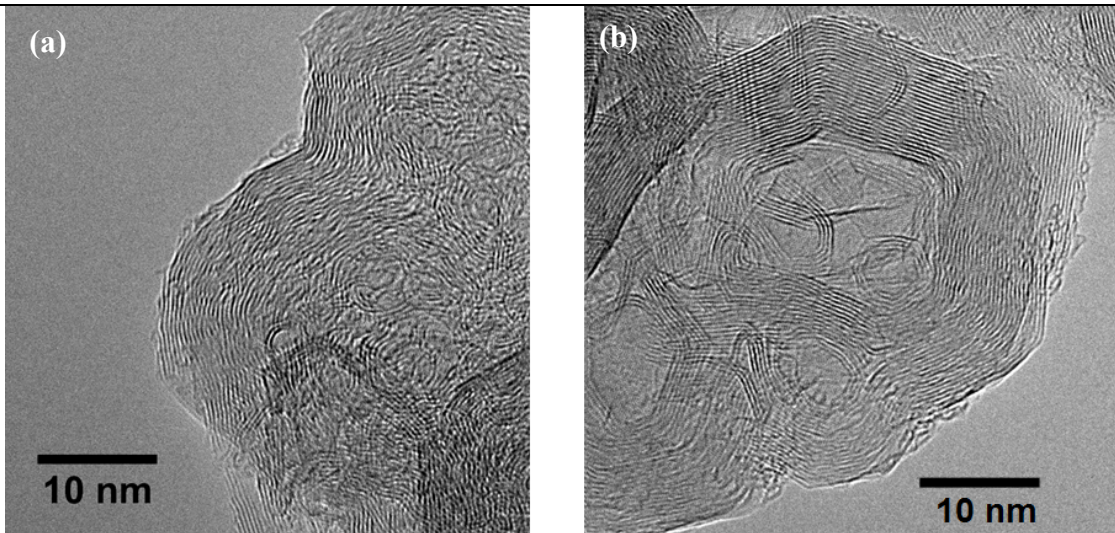


Fig. 3. TEM images of carbon black powder samples: (a) AB and (b) G-AB.

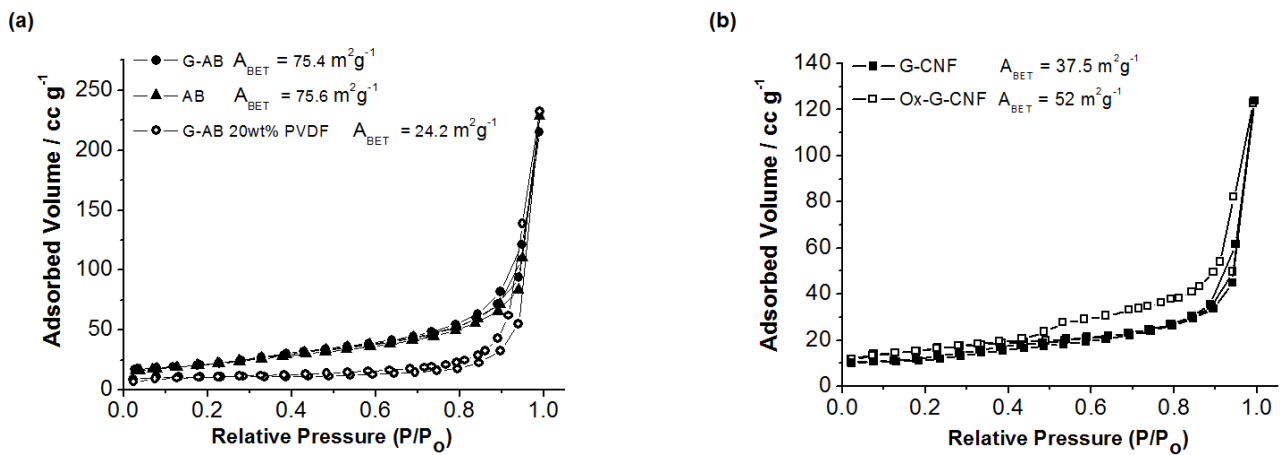


Fig. 4. N₂ adsorption-desorption isotherms of (a) carbon black powder and electrode samples (b) carbon nanofiber powder samples.

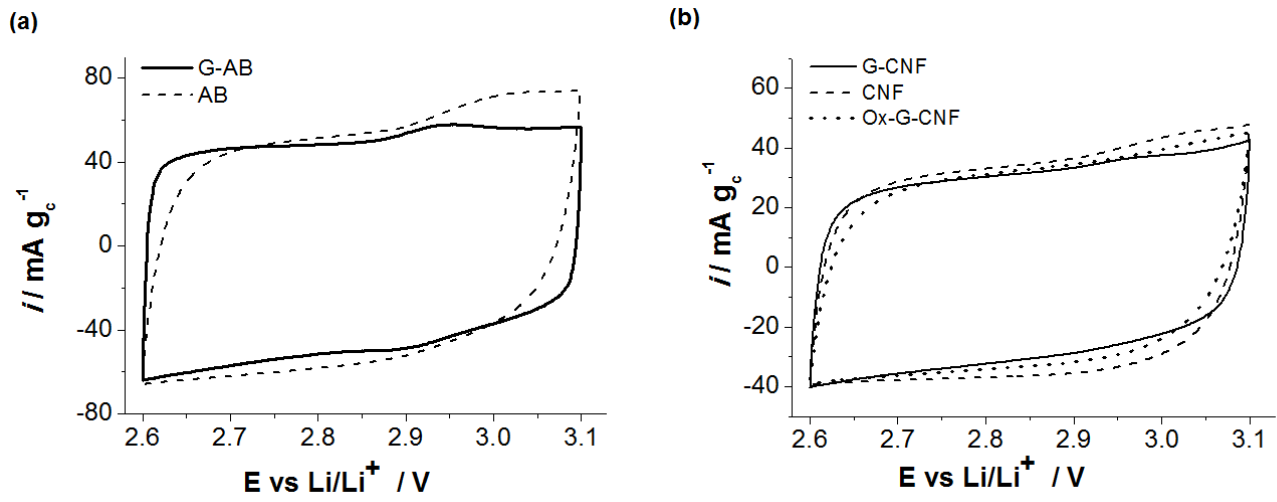


Fig. 5. Cyclic voltammograms for (a) carbon black and (b) carbon nanofiber electrodes with 20wt% of PVDF binder in Ar-saturated 0.1 M LiClO_4 in DME electrolyte. The current is normalized to the carbon mass in the electrode.

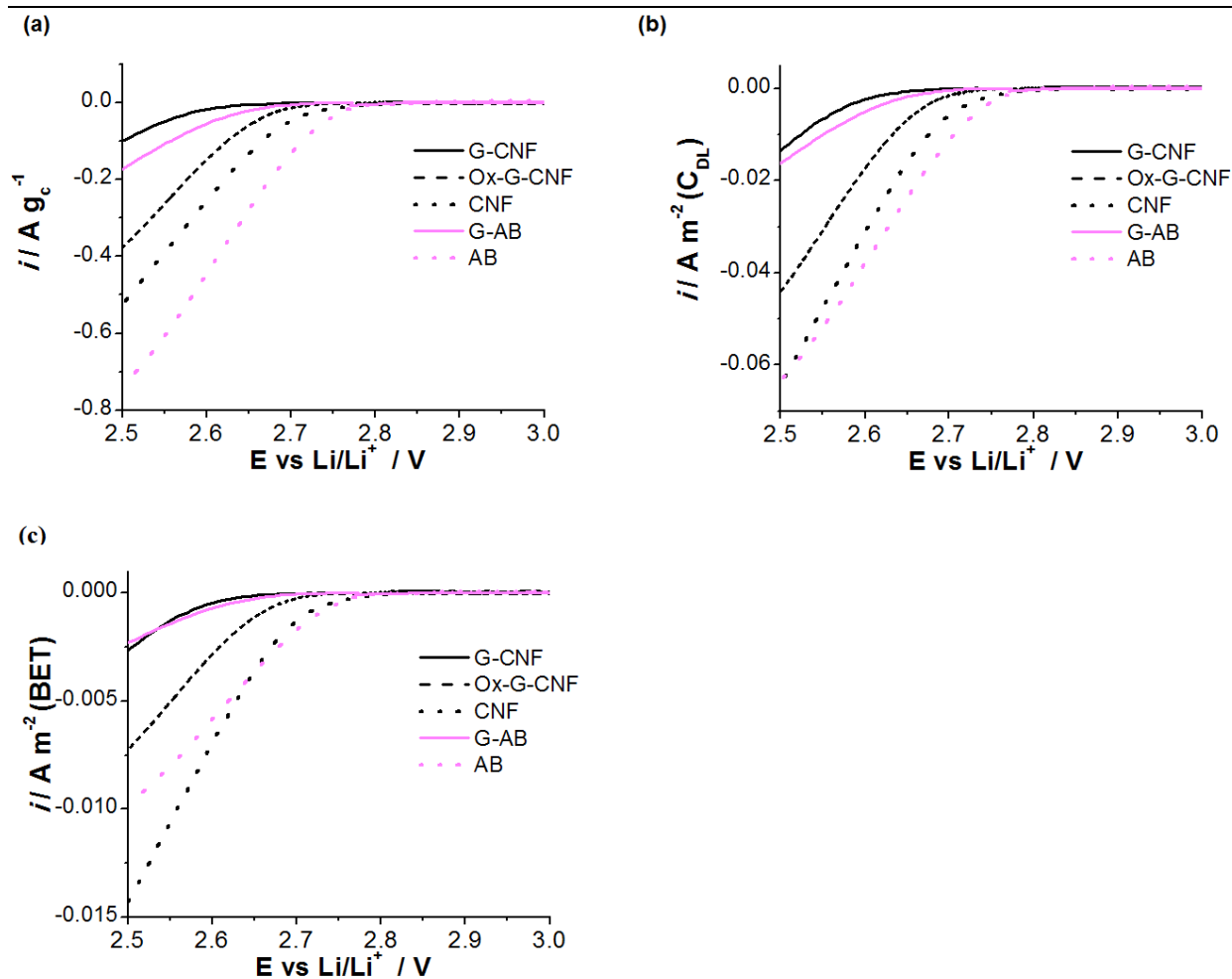


Fig. 6. Linear sweep voltammetry data of O_2 reduction in 0.1M $LiClO_4$ /DME electrolyte at 0.1 mVsec^{-1} for carbon black and carbon nanofiber cathodes with the current i normalized to the (a) carbon mass (b) A_{CDL} of the electrode and (c) A_{BET} of the carbon powder. During measurements, the cells were under a constant flow of O_2 at $0.015 \text{ ml min}^{-1}$ at 298 K.

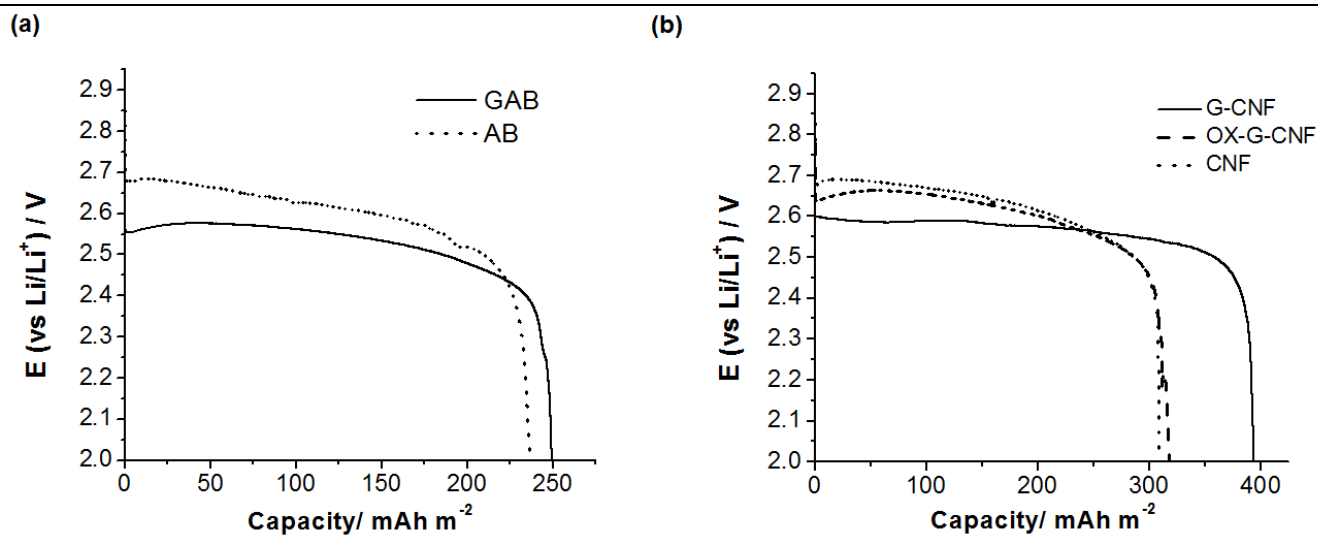


Fig. 7. A_{CDL} -normalized discharge profiles of (a) carbon black cathodes and (b) carbon nanofiber cathodes at 50 mA g_c^{-1} constant current with 0.1 M LiClO_4 in DME electrolyte under a constant flow of O_2 at $0.015 \text{ mL min}^{-1}$ at 298 K . The gravimetric discharge capacities are $2670 \text{ mAh g}_c^{-1}$ and $2768 \text{ mAh g}_c^{-1}$ for GAB and AB, and $2916 \text{ mAh g}_c^{-1}$, $2720 \text{ mAh g}_c^{-1}$ and $2531 \text{ mAh g}_c^{-1}$ for G-CNF, OX-G-CNF and CNF respectively.

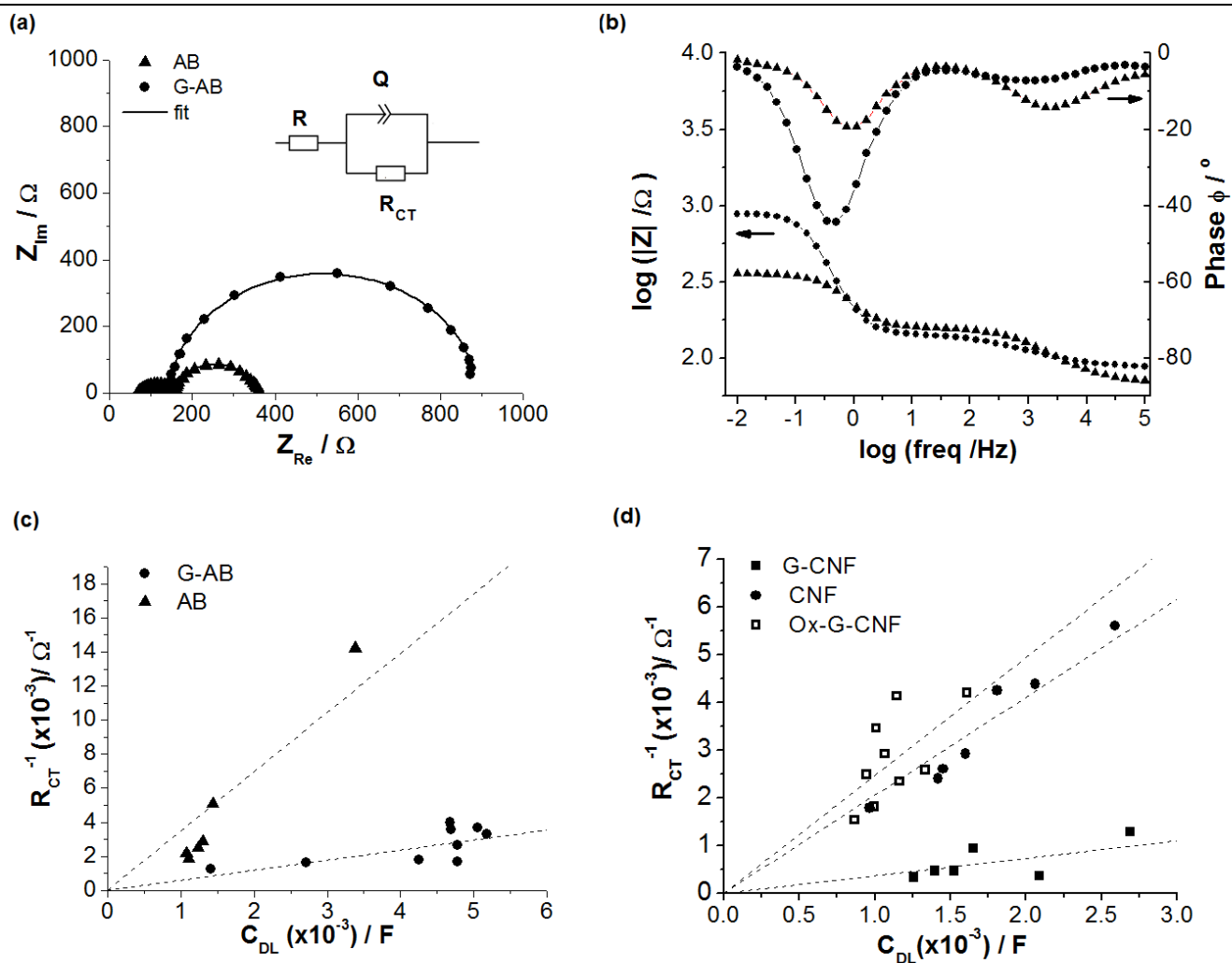


Fig. 8- EIS measurements at constant potential of 2.6 V (vs. Li/Li^+) for AB and G-AB carbon black cathodes presented with the (a) Nyquist plot and (b) Bode plot. The carbon mass in each measurement is ~ 0.6 mg. The plot of inverse charge transfer resistance R_{CT}^{-1} over double layer capacitance C_{DL} obtained from EIS measurements for (c) carbon black cathodes and (d) carbon nanofiber cathodes with different carbon masses. The inset in (a) equivalent circuit to fit the impedance spectra. R: Solution Resistance Q: Constant Phase Element. R_{CT} : Charge Transfer Resistance.